

Quantum order by disorder in Frustrated Spin Nanotubes

João C. Getelina,¹ Zekun Zhuang,² Premala Chandra,² Piers Coleman,^{2,3} Peter P. Orth,^{1,4,5} and S. L. Sondhi⁶

¹*Ames National Laboratory, Ames, Iowa 50011, USA*

²*Center for Materials Theory, Rutgers University, Piscataway, New Jersey 08854, USA*

³*Department of Physics, Royal Holloway, University of London, Egham, Surrey TW20 0EX, UK*

⁴*Department of Physics and Astronomy, Iowa State University, Ames, Iowa 50011, USA*

⁵*Department of Physics, Saarland University, 66123 Saarbrücken, Germany*

⁶*Rudolf Peierls Center for Theoretical Physics, University of Oxford, Oxford OX1 3PU, UK*

(Dated: March 10, 2023)

We investigate quantum order by disorder in a frustrated spin nanotube formed by wrapping a J_1 - J_2 Heisenberg model at 45° around a cylinder. Using Schwinger boson theory and Density Matrix Renormalization Group (DMRG), we have computed the ground-state phase diagram to reveal a \mathbb{Z}_2 phase in which collinear spin stripes form a right or left handed helix around the nanotube. We have derived an analytic estimate for the critical $\eta_c = J_1/2J_2$ of the \mathbb{Z}_2 helical phase transition, which is in agreement with the DMRG results. By evaluating the entanglement spectrum and nonlocal string order parameters we discuss the topology of the \mathbb{Z}_2 -helical phase.

I. INTRODUCTION

Spin models are “economy” strongly correlated systems where fluctuations driven by frustrated interactions result in rich physical phenomena and phase diagrams. Conceptual advances in many-body physics often arise from studies of spin models. One popular example is the emergence of order by disorder in frustrated spin models [1–4], which describes the mechanism by which quantum or thermal fluctuations lift a degeneracy of the ground state in favor of states with discrete [5–13] or algebraic orderings [14–17]. Often studied in the context of Heisenberg spin models, order by disorder occurs in a wide range of strongly correlated systems with competing interactions [17–25]. This physics is well understood within a renormalization group approach: the conventional scaling picture of magnetism incorporates *all* fluctuations into an effective Landau-Ginzburg action for the long-wavelength modes of the spin system. Even when such an action is well-defined, high-energy, short-wavelength spin fluctuations can modify its behavior at long distances. The role of such short-wavelength fluctuations is particularly enhanced in frustrated spin systems with large ground state degeneracies. Here the associated fluctuation free energy often selects maximum entropy states that break lattice symmetries to develop discrete order.

A class model of order by disorder is the spin- $\frac{1}{2}$ $J_1 - J_2$ Heisenberg model on the two-dimensional (2D) square lattice. A predicted finite-temperature Ising nematic phase transition in this model [5] has been computationally confirmed for the classical spin model several years ago [7]. At the Ising nematic transition the four-fold rotation symmetry of the square lattice is broken down to a twofold rotation via the development of a local composite bond order parameter describing the relative orientation of spins. For the quantum spin-1/2 model, the transition has only recently been verified using an $SU(2)$ -invariant finite temperature tensor network algorithm [26], where both quantum and thermal fluctua-

tions are present. Indeed prior series expansion studies suggested that it might be suppressed due to quantum fluctuations [27, 28]. This emergent nematic transition has found analogues in other spin systems [8, 11–13, 29] and unexpected realization in the iron-based superconductors [30–33], where it induces a nematic structural transition in the absence of long-range magnetic order. It has also been identified in several other strongly correlated materials [17, 34–36].

However, the question of whether there is a zero-temperature analogue of this phenomenon in $1 + 1$ D has remained open to date. Here we study such fluctuation-induced symmetry-breaking in a purely quantum spin system at zero temperature, a J_1 - J_2 spin- S Heisenberg model wrapped around a cylinder forming a frustrated spin nanotube (see Fig. 1). Motivated by the discovery of frustrated spin chain materials [37–40], spin nanotubes have been previously studied with different couplings and boundary conditions, both with and without magnetic field [41–46]. Spin nanotubes can also be regarded as n -leg spin ladders with periodic boundary conditions along the short direction and we point out similarities and differences to previous studies of these systems [47–55]. While fluctuation induced couplings, broken symmetry phases (e.g. in Ref. [55]) and order by disorder have been identified there, our exact J_1 - J_2 nanotube model and the possibility of an emergent \mathbb{Z}_2 -helical transition has not yet been investigated in these systems.

Using complementary analytic and computational approaches, we here identify and characterize fluctuation-induced symmetry breaking in frustrated J_1 - J_2 spin nanotubes, demonstrating that quantum fluctuations alone can sustain transitions into phases with discrete order. Specifically, we find that quantum fluctuations select right and left handed helical states from the degenerate ground state manifold. We determine the $T = 0$ quantum critical point associated with the \mathbb{Z}_2 -helical phase to lie in the universality class of the 2D Ising model. We describe the complete ground state phase diagram for general spin length S using a Schwinger boson method [56] and for

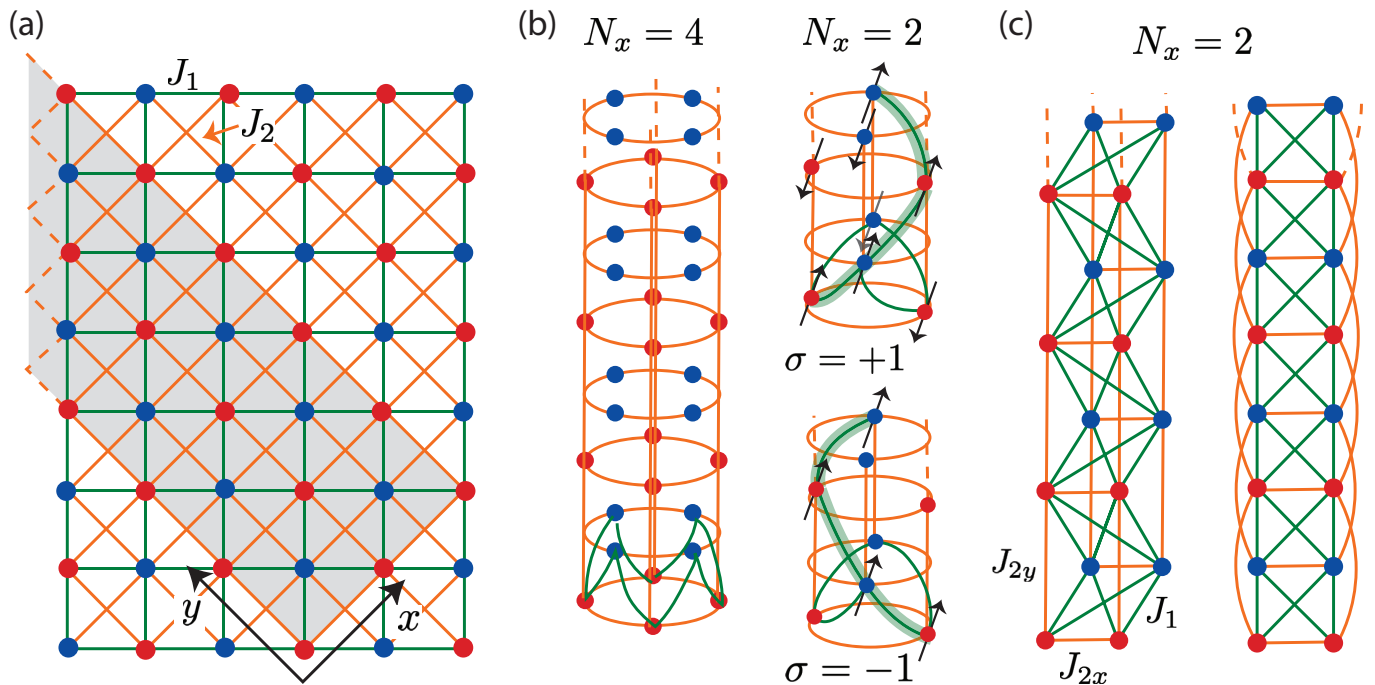


FIG. 1. (a) The J_1 - J_2 square lattice model, where J_1 bonds are shown in green, while J_2 bonds are shown in orange. In the spin nanotube, the J_1 - J_2 model is rotated through 45° and wrapped around a cylinder as shown in (b) for $N_x = 4$ and $N_x = 2$ spins around the circumference. In the $\sigma = \pm 1$ degenerate ground-states, the columns of parallel spins along the J_1 bonds form left- and right-handed helices around the nanotube (thick green). (c) Showing the $N_x = 2$ nanotube recast as a two-leg spin-ladder in which the J_2 bonds in the x and y direction are given values J_{2x} and J_{2y} , respectively.

the case of spin $S = 1/2$ also using the Density Matrix Renormalization Group (DMRG) [57–60]. The results from both methods to be in good qualitative agreement.

We now discuss the modular structure of our paper. In Sec. II, we introduce the frustrated J_1 - J_2 nanotube model. In Sec. III we describe mean-field results for the phase diagrams using a symplectic large- N Schwinger boson method. Complementary Density Matrix Renormalization Group (DMRG) studies for a narrow nanotube and for spin $S = 1/2$ are presented in Sec. IV. We end with a discussion in Sec. V where we summarize the analytic and numerical work and suggest open questions for future research.

II. FRUSTRATED SPIN NANOTUBE MODEL

We consider a 1D analogue of the square lattice J_1 - J_2 model shown in Fig. 1(a) and described by the Hamiltonian

$$H = J_1 \sum_{\langle i,j \rangle} \mathbf{S}_i \cdot \mathbf{S}_j + J_2 \sum_{\langle\langle i,j \rangle\rangle} \mathbf{S}_i \cdot \mathbf{S}_j. \quad (1)$$

Here, $J_1, J_2 > 0$ are fully antiferromagnetic, $\langle i, j \rangle$ sums once over first-neighbor pairs of spins (green bonds), while $\langle\langle i, j \rangle\rangle$ sums over second-neighbor pairs (orange bonds). Blue and red sites in Fig. 1 correspond to the

two interpenetrating second-neighbor square sublattices coupled by J_2 .

Due to the coexistence of J_1 and J_2 coupling, this model is frustrated, lacking a single classical configuration that simultaneously minimizes the energy of all bonds. For the square lattice model in the classical limit, it is known that the ground state consists of two decoupled antiferromagnetic sublattices when the frustration parameter

$$\eta = \frac{J_1}{2J_2} < 1 \quad (2)$$

and exhibits Néel order if $\eta > 1$. Here, we focus on the regime $\eta < 1$. The two antiferromagnetic sublattices are only decoupled in the absence of fluctuations, i.e. at zero temperature and for purely classical spins. Finite quantum or thermal fluctuations couple the two sublattices and select out the collinear states from the classically degenerate ground state manifold via the order by disorder mechanism [1–3, 5, 61]. As noted above, the selection of one of the two collinear states breaks the fourfold lattice rotation symmetry down to a twofold rotation symmetry, which occurs at a finite transition temperature T_c via a continuous phase transition in the 2D Ising universality class [5, 7, 26]. Heuristically, the phase transition occurs when the Heisenberg correlation length becomes comparable to the domain wall thickness separating the \mathbb{Z}_2 domains.

To investigate order by disorder in (1 + 1)D, the simplest modification to the square lattice model is to wrap it around a cylinder to make a spin nanotube. To avoid breaking the \mathbb{Z}_2 diagonal mirror symmetry between the two J_1 bond directions, it is important to rotate the strip by 45 degrees and wrap it along the direction of the J_2 bonds (x -direction), as shown in Fig. 1(a). On the nanotube, this symmetry corresponds to a longitudinal mirror symmetry of the lattice along the infinite direction $y \rightarrow -y$. To avoid extra frustration around the tube in the $J_2 > J_1$ limit, we constrain the number of spins N_x along the x -direction to be even. The model is expected to be gapped for even N_x . Since long-range order is absent at any finite temperature in 1D, we here focus on the ground state at $T = 0$. The strength of quantum fluctuations is controlled by the spin length S and we investigate the ground state phase diagram for different values of S and frustration ratios η . As we will show below, there exists a range of frustration ratios η where the ground state exhibits \mathbb{Z}_2 -helical order although there is no long-range antiferromagnetic order. The emergent \mathbb{Z}_2 -helical order corresponds to a different chirality of the helix that follows the relative orientation of the spins around the nanotube, as depicted in Fig. 1(c). This order is characterized by a local plaquette order parameter which breaks the longitudinal mirror symmetry.

We here focus on narrow nanotubes with $N_x = 2, 4$ sites along the short direction, as shown in Fig. 1. For the minimal length nanotubes with $N_x = 2$, we contrast the situation of a spin nanotube, which exhibits periodic boundary conditions (PBC) along the short direction, with that of a nanostrip, which exhibits open boundary conditions (OBC), we consider two cases: (i) $J_{2,x} = J_{2,y}$, and (ii) $J_{2,x} = 2J_{2,y}$. Case (i) can be regarded as a nanostrip, and case (ii) as a nanotube, where the transverse bond along the short direction is counted twice due to the wrapping around the cylinder [see Fig. 1(c)]. This makes the total J_2 coupling of a site along x and y bonds equal and corresponds to the situation encountered for $N_x > 2$ and the 2D square lattice, where every site has two J_2 neighbors along short and long directions. Importantly, we obtain qualitatively identical results for the nanostrip and nanotube geometries at $N_x = 2$.

III. SCHWINGER BOSON THEORY

A. General formalism

Solving spin models is a formidable task and exact solutions are rare. A useful analytic method represents the quantum spins using Schwinger bosons, an approach which permits a natural generalization in the number of boson flavors from 2 to N . As N becomes large, the Schwinger boson path integral is dominated by its saddle-point and the problem becomes exactly solvable in the large N limit. At finite N this approach provides a controlled expansion of the small parameter $1/N$

using diagrammatic methods[62]. The natural extension of the Schwinger boson symmetry group of from $SU(2)$ to $SU(N)$ group originally introduced by Arovav and Auerbach is limited to ferromagnets and bipartite antiferromagnets [63]. To treat frustrated antiferromagnets, Sachdev and Read developed the $SP(N)$ approach [64], which however tends to underestimate the ferromagnetic correlations between the frustrated spins. In this work, we follow the symplectic- N approach formalized by Flint and Coleman [56], which treats antiferromagnetic and ferromagnetic correlations on an equal footing.

In the symplectic- N formalism, the $SU(2)$ spin generators S^α are generalized to the generators T^α of $SP(N)$ ($N = 2, 4, \dots$), and the general Hamiltonian takes form

$$H = \sum_{i,j} \frac{J_{ij}}{N} \mathbf{T}_i \cdot \mathbf{T}_j. \quad (3)$$

The $SP(N)$ generators can be represented with Schwinger bosons $T^\alpha = b_{\sigma'}^\dagger (T^\alpha)_{\sigma\sigma'} b_{\sigma'}$, where the spin index takes the values $\sigma = \pm 1, \pm 2, \dots \pm \frac{N}{2}$. Using the completeness relation $\sum_\alpha (T^\alpha)_{ab} (T^\alpha)_{cd} = \frac{1}{4}(\delta_{ad}\delta_{bc} - \epsilon_{ac} \epsilon_{bd})$, where $\epsilon_{ab} = \text{sgn}(a)\delta_{a,-b}$, the Hamiltonian becomes

$$H = \sum_{i,j} \frac{J_{ij}}{N} \left[A_{ij}^\dagger A_{ij} - B_{ij}^\dagger B_{ij} \right], \quad (4)$$

where $A_{ij}^\dagger = \frac{1}{2} \sum_\sigma b_{i\sigma}^\dagger b_{j,\sigma}$ describe normal bosonic bilinears and $B_{ij}^\dagger = \frac{1}{2} \sum_\sigma \text{sign}(\sigma) b_{i\sigma}^\dagger b_{j,-\sigma}^\dagger$ describe anomalous ones. One can express the partition function using path integrals with the constraint $\sum_\sigma b_{i,\sigma}^\dagger b_{i,\sigma} = NS$ enforced by adding a Lagrange multiplier term $\exp(-\lambda_i (\sum_\sigma b_{i,\sigma}^\dagger b_{i,\sigma} - NS))$. After making the Hubbard-Stratonovich transformation, one obtains the saddle-point solution, which becomes exact in the large N limit. This procedure is in fact equivalent to a mean-field treatment of Eq. (4), which becomes

$$H_{\text{MF}} = \sum_{i,j} \left[\bar{h}_{ij} A_{ij} + A_{ij}^\dagger h_{ij} - \bar{\Delta}_{ij} B_{ij} - B_{ij}^\dagger \Delta_{ij} \right] \quad (5)$$

$$- \frac{N}{J_{ij}} \bar{h}_{ij} h_{ij} + \frac{N}{J_{ij}} \bar{\Delta}_{ij} \Delta_{ij} \Big] + \sum_{i,\sigma} \lambda_i (b_{i,\sigma}^\dagger b_{i,\sigma} - S)$$

with self-consistent conditions $\sum_\sigma \langle b_{i,\sigma}^\dagger b_{i,\sigma} \rangle = NS$, $h_{ij} = \frac{J_{ij}}{N} \langle A_{ij} \rangle$ and $\Delta_{ij} = \frac{J_{ij}}{N} \langle B_{ij} \rangle$. Alternatively, one could also determine the mean-field parameters by requiring $\partial E_g / \partial h = \partial E_g / \partial \Delta = \partial E_g / \partial \lambda = 0$, where E_g is the ground state energy. Since the Hamiltonian H_{MF} contains $N/2$ equivalent copies of Kramers doublet, it is only necessary to focus on the Hamiltonian \tilde{H} of a single copy, which can be written in a compact form

$$\tilde{H} = \sum_{i,j} \Psi_i^\dagger H_{ij} \Psi_j + \lambda_i (\Psi_i^\dagger \Psi_i - 2S - 1) \quad (6)$$

$$+ \sum_{i,j} \left[\frac{2}{J_{ij}} \bar{\Delta}_{ij} \Delta_{ij} - \frac{2}{J_{ij}} \bar{h}_{ij} h_{ij} \right], \quad (7)$$

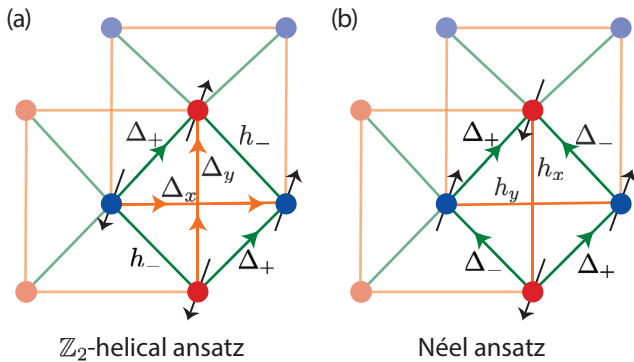


FIG. 2. Schwinger boson mean-field ansätze used in this work, where Δ defines the strength of the (antiferromagnetic) pairing and h the strength of the (ferromagnetic) particle-hole hybridization. Since $\Delta_{ij} = -\Delta_{ji}$ along the antiferromagnetic bonds, to avoid ambiguity the arrow points to the designated “ i ” site on the bond. (a) \mathbb{Z}_2 -helical ansatz and (b) Néel ansatz.

where we define Nambu spinor $\Psi_i^\dagger = (b_{i\uparrow}^\dagger, b_{i\downarrow}^\dagger)$ and

$$H_{ij} = \begin{pmatrix} h_{ij} & -\Delta_{ij} \\ \bar{\Delta}_{ij} & \bar{h}_{ij} \end{pmatrix}. \quad (8)$$

B. Mean-field phase diagrams

In principle, the mean-field states of Eq. (1) can be obtained by minimizing the ground state energy of Eq. (7) with respect to all possible mean-field parameters, which is generally rather difficult. Here we only consider translationally invariant mean-field ansätze that are connected to the \mathbb{Z}_2 ansatz or Néel ansatz, as shown in Fig. 2, via second-order phase transitions. The first-order phase transition is then determined by directly comparing the ground state energy of different states, while the continuous phase transition is determined by analyzing the instability of ground state energy through the calculation of its second derivatives. Below we show our final results and the detailed calculations can be found in Appendix A.

Figure 3 shows the mean-field phase diagram of $N_x = 4$ spin nanotube. For $0 < \eta < 1$, the classical ground state of the system contains two decoupled antiferromagnetic sublattices (DAS). When S is large but finite, the quantum fluctuation removes the classical degeneracy and leads to \mathbb{Z}_2 -helical long-range order (LRO), which corresponds to different handedness of spin texture around the nanotube (see Fig. 1(b)). When η or S decreases, the enhanced quantum fluctuation melts the order and the system continuously transitions to the DAS phase. At intermediate η , there exists a ‘decoupled antiferromagnetic chain’ (DAC) phase, which exists at unrealistically small S and may be unstable when finite N fluctuation is considered. For sufficiently large η , antiferromagnetic alignment of nearest-neighbor spins is favored, and

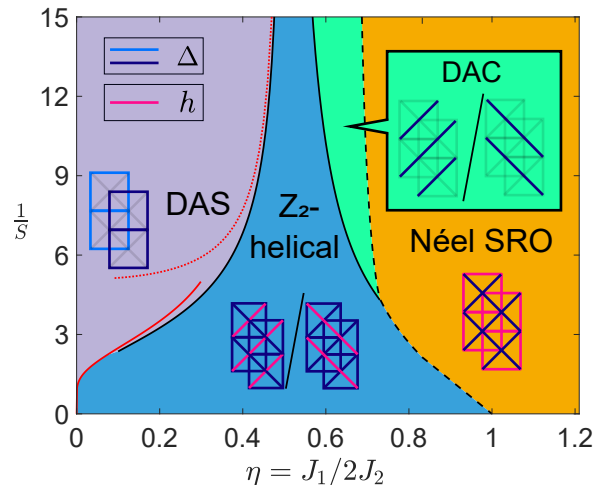


FIG. 3. The phase diagram of $N_x = 4$ spin nanotube predicted by Schwinger boson theory. The black solid (dashed) line represents the second(first)-order phase transition, while the red solid (dotted) line represents the \mathbb{Z}_2 critical line in the one(two)-dimensional limit. Also shown are the valence bond structures of the corresponding mean-field ansätze, where blue lines represent the antiferromagnetic bonds while the violet-red lines denote the ferromagnetic bonds (same for Fig. 4 and Fig. 5).

the system enters Néel short-range order (SRO) phase through a first-order transition.

For general $N_x \geq 4$, the phase diagram is expected to be similar to the $N_x = 4$ case. Near the \mathbb{Z}_2 phase transition, the system may be regarded as one-dimensional if the spin correlation length is much larger than the circumference of the nanotube ($\eta \rightarrow 0$), or two-dimensional if in the opposite limit ($\eta \rightarrow 1/2$). The asymptotic solution of the second-order phase transition in the 1D regime is given by

$$S_{\text{ch}} \exp\left(-\frac{N_x \pi (S_{\text{ch}} + 1/2)}{\sqrt{2}}\right) = \frac{\sqrt{\gamma_N} \eta}{16 N_x \pi}, \quad (9)$$

where γ_N is a N_x -dependent constant (see Appendix A). In the 2-D regime, the critical line for the spin nanotube becomes asymptotic to that in the exact two dimensions. From Fig. 3 one can see that when η gets closer to zero, the analytic solution (9) agrees better with the exact numerical result; while when η is close to $1/2$, the difference of S_{ch} between the two-dimensional system ($N_x = \infty$) and one-dimensional nanotube (finite N_x) vanishes. One expects that when N_x increases, a larger range of \mathbb{Z}_2 transition line will coincide with that of the two-dimensional system, while a narrower range of \mathbb{Z}_2 transition can be described by the Eq. (9), and the system makes crossover from 1D to 2D at a smaller value of η .

We now demonstrate the special case $N_x = 2$ where the system may be regarded as a two-leg ladder. For the spin nanostrip ($J_{2,x} = J_{2,y}$), the phase diagram shares

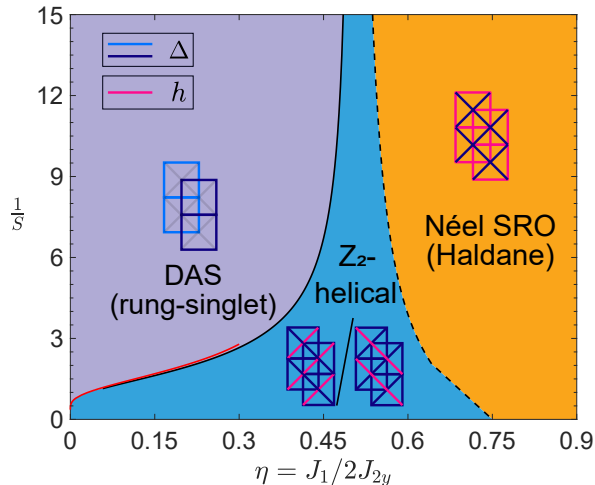


FIG. 4. The phase diagram of $N_x = 2$ spin nanostrip, i.e. case (i) $J_{2,x} = J_{2,y}$, predicted by Schwinger boson theory. The black solid (dashed) line represents the second(first)-order phase transition, while the red solid line is the analytic solution Eq. (10).

many similarities with that of the $N_x = 4$ case, as shown in Fig. 4. The critical line when $\eta \rightarrow 0$ is given by the asymptotic solution

$$S_{\text{ch}} \exp\left(-\frac{2\sqrt{6}\pi(S_{\text{ch}} + 1/2)}{3}\right) = \frac{\sqrt{\gamma'_2}\eta}{32\pi}, \quad (10)$$

where $\gamma'_2 = 8\left[\frac{2}{3} - \sqrt{\frac{2}{3}} \ln(\sqrt{2} + \sqrt{3})\right] \approx 2.15$. For $S = 1/2$ the \mathbb{Z}_2 order phase exists when $0.22 < \eta < 0.65$, while for $S = 1$ the \mathbb{Z}_2 order phase exists when $0.03 < \eta < 0.7$.

The phase diagram of the $N_x = 2$ spin nanotube ($J_{2,x} = 2J_{2,y}$) is somewhat distinct from that of the other cases, as seen from Fig. 5. The main difference is that there also exists a valence-bond solid phase, which nevertheless occurs only for unrealistically small spin $S < 0.21$. The emergence of this phase can be understood by noting that, the J_2 coupling between two sites in the x direction is twice larger than those in the y direction, which hence favors the formation of transverse valence bonds. Nevertheless, the asymptotic solution of \mathbb{Z}_2 critical line has a similar form

$$S_{\text{ch}} e^{-\sqrt{2}\pi(S_{\text{ch}} + 1/2)} = \frac{\sqrt{\gamma_2}\eta}{32\pi}, \quad (11)$$

where $\gamma_2 = 8(\sqrt{2} \ln(\sqrt{2} + 1) - 1) \approx 1.97$. The \mathbb{Z}_2 order phase exists when $0.53 < \eta < 0.91$ for spin-1/2 system, while it exists when $0.12 < \eta < 0.96$ for spin-1 system.

Our results Eqs. (9)(11) may be understood in a similar way as done by Chandra *et al.* for the \mathbb{Z}_2 transition driven by thermal fluctuation in two dimensions [5]: the \mathbb{Z}_2 order exists when the 1-D Heisenberg correlation length ξ is larger than the \mathbb{Z}_2 domain wall width w_{DW} , and a simple estimate gives $\xi \sim \exp(N_x \pi(S + 1/2)/\sqrt{2})$,

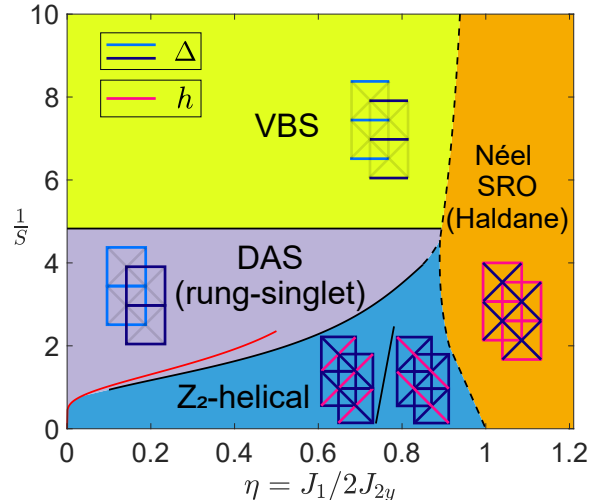


FIG. 5. The phase diagram of $N_x = 2$ spin nanotube, i.e. case (ii) $J_{2,x} = 2J_{2,y}$, predicted by Schwinger boson theory. The black solid (dashed) line represents the second(first)-order phase transition, while the red solid line is the analytic solution Eq. (11).

$w_{\text{DW}} \sim J_2/J_1$. Therefore, the \mathbb{Z}_2 phase transition occurs when $\exp(-N_x \pi(S + 1/2)/\sqrt{2}) \sim \eta$. Note that compared to this estimate, our results (see Eq. (9)) based on Schwinger boson approach has an extra spin-dependent factor, which has also been seen in a similar Schwinger boson calculation of 2-D \mathbb{Z}_2 phase transition at finite temperature [56]. We speculate such difference is due to the negligence of finite N fluctuation in the mean-field approach and expect such difference to be eliminated when the fluctuations are taken into account.

IV. DMRG RESULTS

A. Model and simulation parameters

In this section we present DMRG simulation results for the spin-1/2 nanotube. We focus on nanotubes with the minimal length $N_x = 2$ along the short direction, as shown in Fig. 1. We choose a unit cell vector a_y such that the 1D model contains four basis sites per unit cell, two "blue" and two "red" sites [see Fig. 6(a)]. As mentioned before, blue and red sites correspond to the two interpenetrating second-neighbor square sublattices coupled by J_2 . We denote the total number of unit cells by L_y , and the model thus contains $N = 4L_y$ spins. We consider two values for the ratio $J_{2,x}/J_{2,y}$, where $J_{2,x}$ describes the coupling along the rungs, and $J_{2,y}$ is the second-neighbor coupling along the chains. We refer to case (i) $J_{2,x} = J_{2,y}$ as the nanostrip, and to case (ii) $J_{2,x} = 2J_{2,y}$, where the transverse bond along the short direction is counted twice due to the wrapping around the cylinder.

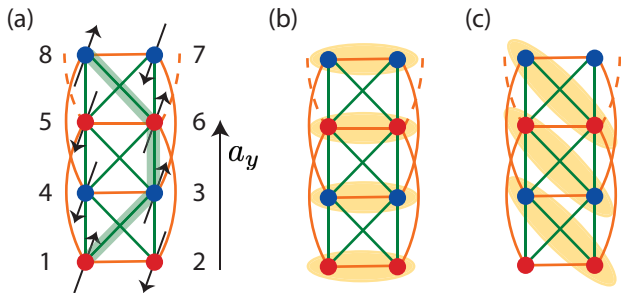


FIG. 6. (a) Site labeling used in DMRG calculations. Order parameter σ_i of the \mathbb{Z}_2 -helical phase explicitly reads for the first double plaquette $\sigma_1 = (\mathbf{S}_3 - \mathbf{S}_4) \cdot (\mathbf{S}_1 - \mathbf{S}_2 + \mathbf{S}_6 - \mathbf{S}_5)$. Thick green bonds follow parallel spins. We use the unit cell vector a_y such that there are four spins per unit cell. The total number of spins in the model is given by $N = 4L_y$, where L_y is the total number of plaquettes. (b) Pairing of spins-1/2 in the odd string order parameter $\mathcal{O}_{\text{odd}}^z$ in Eq. (16) (c) Pairing of spins in the even string order parameter $\mathcal{O}_{\text{even}}^z$ in Eq. (17).

We use the Julia simulation library iTensor [60, 65] to perform the DMRG calculations in this work. For each DMRG run we allow for up to 30 sweeps, with only the final sweep being truncated at a discarded weight of maximally 10^{-10} . The maximum bond dimension m is doubled after every three sweeps, and we set a final value of $m = 3840$ for the final truncated sweep. We consider open BCs along the long direction with a total number of L_y unit cells. The labeling of the sites follows a snake-like pattern, as shown in Fig. 6(a).

The DMRG simulations are set to be quantum-number conserving, which reduces the simulation time. For spin chains the conserved quantum number corresponds to the z -component of the total spin S_{tot}^z . When computing the spin gap, we perform two DMRG runs for each system size L_y , one in the sector with $S_{\text{tot}}^z = 0$, and another one in the sector with $|S_{\text{tot}}^z| = 1$. After determining the ground state in each total spin sector, we also find the first-excited states in each total spin sector from a second DMRG run, where we add a penalty term to the Hamiltonian that is the weighted projection to the previously determined ground state.

To directly observe the emergence of \mathbb{Z}_2 -helical order we measure a suitable plaquette bond order parameter σ . For the site labeling in Fig. 6(a), we define the order parameter as

$$\sigma(L_y) = \frac{1}{8(L_y - 1)S(S + 1)} \sum_{i=1}^{L_y-1} \sigma_i, \quad (12)$$

where the bond order parameter at plaquette i reads

$$\sigma_i = (\mathbf{S}_{4i-1} - \mathbf{S}_{4i}) \cdot (\mathbf{S}_{4i-3} + \mathbf{S}_{4i+2} - \mathbf{S}_{4i-2} - \mathbf{S}_{4i+1}). \quad (13)$$

Here, the spin operators can be expressed in terms of Pauli matrices as $\mathbf{S}_i = \frac{1}{2}(X_i, Y_i, Z_i)$. We note that the

normalization is chosen such that $\sigma = 1/3$ in the Z basis Néel product state $|\uparrow\downarrow\uparrow\downarrow\uparrow\downarrow\uparrow\downarrow\cdots\rangle$, where the sites are increasing from left to right starting from $i = 1$ and $Z|\uparrow\rangle = |\uparrow\rangle$, $Z|\downarrow\rangle = -|\downarrow\rangle$. Also note that the summation in Eq. (12) only runs until $i = L_y - 1$, because we use a lattice geometry with an equal number of “blue” and “red” sites, and the top row of spins is thus “blue”.

The initial state of the DMRG simulations is chosen to be a Z basis Néel product state for each sublattice. If the first site of the “blue” sublattice (site $i = 3$) has the same spin direction as the first site of the “red” sublattice (site $i = 1$), i.e., $|\uparrow\downarrow\uparrow\downarrow\uparrow\downarrow\uparrow\downarrow\cdots\rangle$, the initial state has $\sigma = 1/3$. In contrast, if they are in antiparallel directions, i.e., $|\uparrow\downarrow\uparrow\downarrow\uparrow\downarrow\uparrow\downarrow\cdots\rangle$, then we find $\sigma = -1/3$. In cases where $\sigma \neq 0$, we have verified that the final converged state at the end of the DMRG simulation shares the same σ sign as the initial state. By preparing different Néel product initial states, we have also explicitly checked that the two states with opposite σ signs are energetically degenerate. However, the DMRG method can still return a state that is a superposition of the two possible symmetry breaking states. In order to avoid converging into a superposition of symmetry-broken states, we added an external symmetry-breaking pinning field at the top and bottom boundary plaquettes

$$H_\lambda = \lambda [\sigma_1 + (\mathbf{S}_{N-3} - \mathbf{S}_{N-2}) \cdot (\mathbf{S}_{N-5} + \mathbf{S}_N - \mathbf{S}_{N-4} - \mathbf{S}_{N-1})]. \quad (14)$$

In the following, we use a pinning field of strength $\lambda = 1$, except where explicitly noted. To still be able to observe the behavior free of the pinning field, one can apply the subtraction method as described in Ref. [59].

B. Phase diagram and energy gap

In this section, we determine the \mathbb{Z}_2 -helical order parameter and the energy gap above the (possibly degenerate) ground state as a function of $J_1/(2J_{2y})$. This directly establishes the presence of a \mathbb{Z}_2 -helical phase with a nonzero local order parameter in the system. In Fig. 7(a, b), we show the order parameter σ in the converged DMRG ground state for different $\eta = J_1/(2J_{2y})$ and system sizes up to $L_y = 128$. Panel (a) corresponds to the nanostrip case $J_{2x} = J_{2y}$, and (b) to the nanotube $J_{2x} = 2J_{2y}$. We obtain our results starting from an initial Néel product state $|\uparrow\downarrow\cdots\rangle$ with $\sigma = 1/3$ and in the presence of a boundary pinning field $\lambda = 1$. The inset displays the order parameter in the thermodynamic limit, which is obtained by extrapolating the results $\sigma(L_y)$ to $1/L_y \rightarrow 0$. The blue shaded area thus represents the \mathbb{Z}_2 -helical phase, which is characterized by a nonzero local order parameter σ_∞ . We note that we are using the “subtraction method” formula to remove boundary effects in

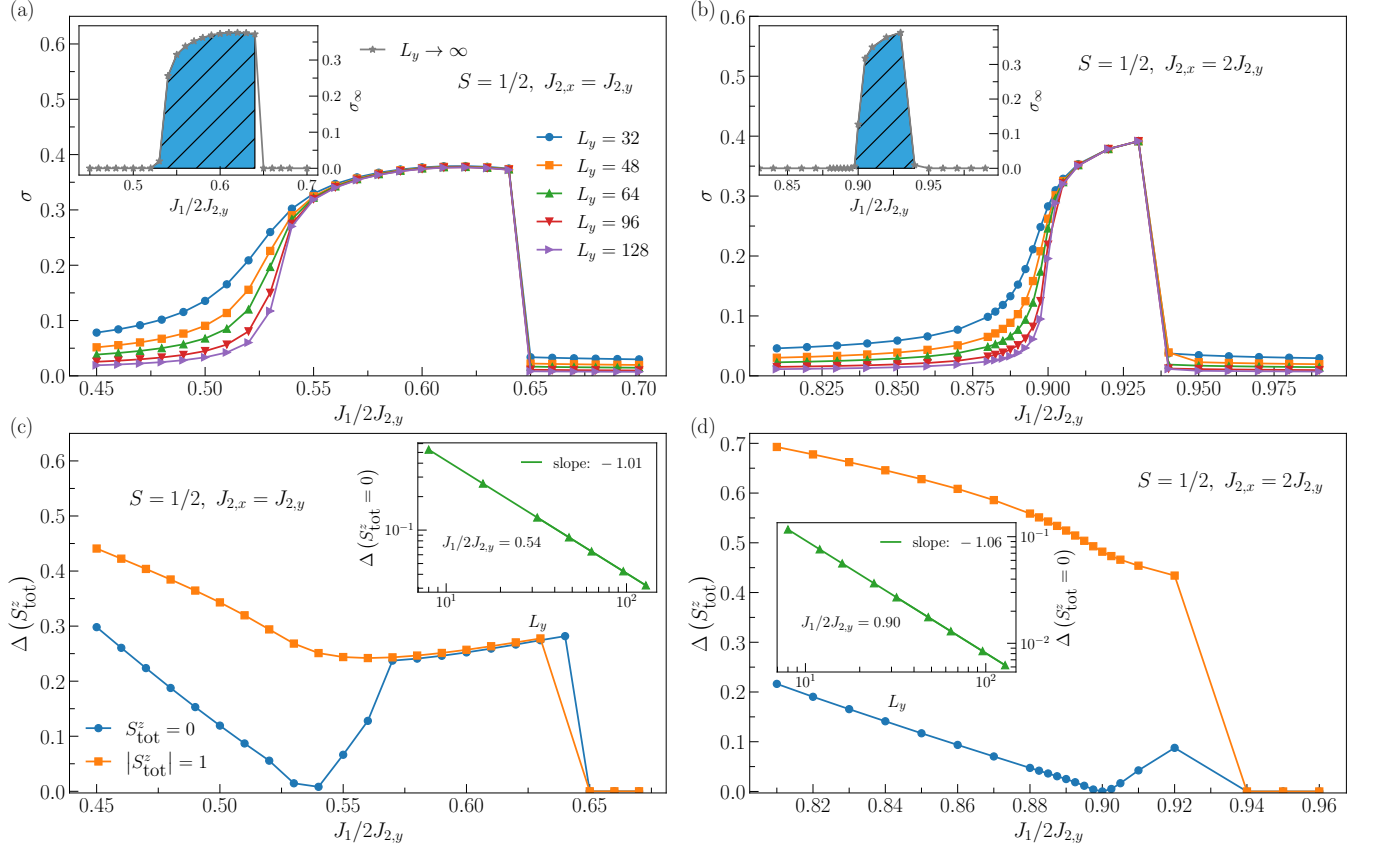


FIG. 7. Upper panels: \mathbb{Z}_2 -helical order parameter σ as a function of $\eta = J_1/2J_2$ for $S = 1/2$, $N_x = 2$ and various cylinders of length L_y . The inset shows the value of σ extrapolated to $L_y \rightarrow \infty$. Lower panels: Bulk system energy difference Δ between the ground and first-excited states in the sector $S_{\text{tot}}^z = 0$ (circles), and between the ground states of sectors $|S_{\text{tot}}^z| = 1$ and $S_{\text{tot}}^z = 0$ (squares). Left and right-hand side panels correspond to cases $J_{2,x} = J_{2,y}$ and $J_{2,x} = 2J_{2,y}$, respectively.

the finite L_y results [59]:

$$\sigma_\infty(L_y^{(1)}, L_y^{(2)}) = \frac{2S(S+1)}{L_y^{(2)} - L_y^{(1)}} \left[(L_y^{(2)} - 1)\sigma(L_y^{(2)}) - (L_y^{(1)} - 1)\sigma(L_y^{(1)}) \right]. \quad (15)$$

Comparing panels (a) and (b), we observe that the \mathbb{Z}_2 -helical phase is wider and centered at a smaller value of η for the nanostrip case $J_{2,x} = J_{2,y}$ (panel a). This is consistent with our results using Schwinger boson theory (cf. Figs. 4 and 5).

The \mathbb{Z}_2 -helical phase extends over a range $\eta_{c,1} \leq \eta \leq \eta_{c,2}$. We find the phase boundary on the left to be at $\eta_{1,c} = 0.540(5)$ for the nanostrip and $\eta_{c,1} = 0.902(5)$ for the nanotube. The boundary on the right occurs at $\eta_{c,2} = 0.650(5)$ for the nanostrip and at $\eta_{c,2} = 0.940(5)$ for the nanotube. While the order parameter smoothly vanishes at $\eta_{c,1}$, it abruptly drops to zero at $\eta_{c,2}$. This suggests the presence of a continuous phase transition at $\eta_{c,1}$, but a first order transition at $\eta_{c,2}$. This will be confirmed by our detailed numerical study below, where we also show that the continuous phase transition at $\eta_{c,1}$ lies in the universality class of the 2D Ising model.

In Figs. 7(c, d), we present the energy gap above the ground state as a function of η . Panel (c) is for the nanostrip and panel (d) is for the nanotube. Before discussing the results, it is important to note that the degeneracy of the ground state changes as we vary η . While the ground state is singly degenerate for $\eta < \eta_{c,1}$, we find it to be twofold degenerate within the \mathbb{Z}_2 -helical phase for $\eta_{c,1} < \eta < \eta_{c,2}$. In both cases the ground state lies in the sector $S_{\text{tot}}^z = 0$. Finally, it is fourfold degenerate for $\eta > \eta_{c,2}$ with two ground states lying in the $S_{\text{tot}}^z = 0$ sector and the other two in the $|S_{\text{tot}}^z| = 1$ sectors.

Figs. 7(c, d) contain two energy gap curves: one is the energy gap between the first-excited and the ground state of sector $S_{\text{tot}}^z = 0$ (blue), and the other one is the energy difference between the ground states of sectors $|S_{\text{tot}}^z| = 1$ and $S_{\text{tot}}^z = 0$ (orange). The shown gap values are obtained by fitting gap results for various cylinder lengths L_y to the equation $f(\mathbf{a}, L_y) = \sum_{i=0}^3 a_i (L_y)^{-i}$. We show a scaling plot of the spin gap $\Delta(|S_{\text{tot}}^z| = 1)$ for several η values in see Appendix B.

We find a nonzero energy gap above the doubly degenerate ground state in the \mathbb{Z}_2 -helical phase. The gap to the first excited state in the $S_{\text{tot}}^z = 0$ sector closes smoothly

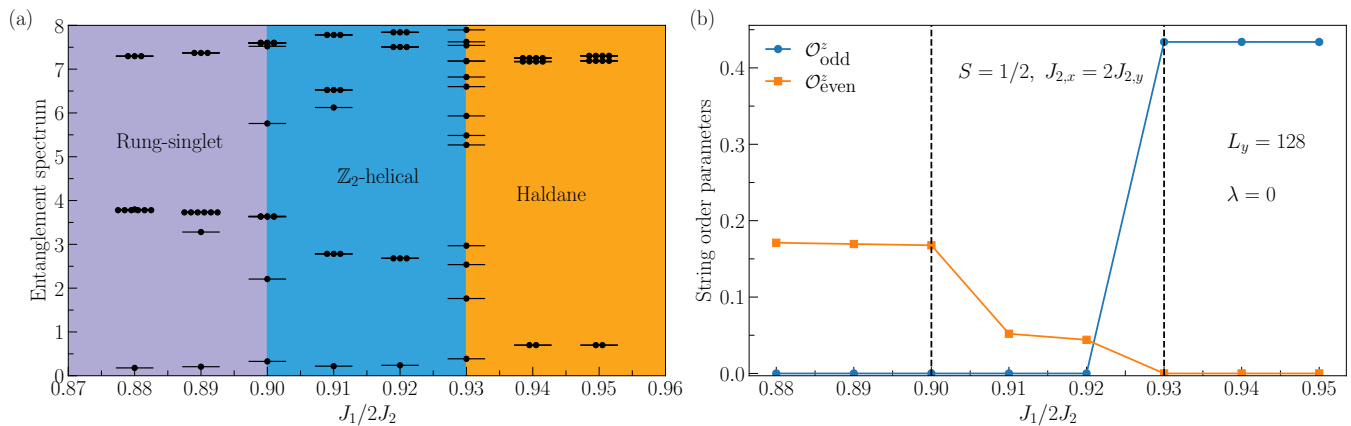


FIG. 8. (a) Entanglement spectrum and (b) string order parameters $\mathcal{O}_{\text{odd}}^z$ and $\mathcal{O}_{\text{even}}^z$ as a function of $\eta = J_1/2J_2$ for a nanotube with $J_{2,x} = 2J_{2,y}$ and length $L_y = 128$ and no pinning field ($\lambda = 0$). The dashed line in panel (b) denotes the \mathbb{Z}_2 -helical phase.

at $\eta_{c,1}$. The insets show the (singlet) gap at $\eta_{c,1}$ versus system size, which follows a power law $\Delta(S_{\text{tot}}^z = 0 \propto L_y^{-z}$ with exponent $z = 1$. This is consistent with the 2D Ising universality class. The gap reopens for $\eta < \eta_{c,1}$, where we find a singly degenerate ground state. The gap to the triplet sector stays nonzero across the critical point. We note that due to $SU(2)$ symmetry, all triplet energies are threefold degenerate, which explains the degeneracy of the blue and orange curves inside the \mathbb{Z}_2 -helical phase in Fig. 7(c).

In contrast, at the first order transition $\eta_{c,2}$ we find that both the singlet and the triplet gap abruptly vanish and the ground state becomes fourfold degenerate. We have checked that it remains gapped above the ground state by calculating the second excited state in the $S_{\text{tot}}^z = 0$ and $|S_{\text{tot}}^z| = 1$ sectors (not shown).

To better understand the two phases that surround the \mathbb{Z}_2 -helical phase, let us investigate the limits $\eta \ll 1$ and $\eta \gg 1$. For $\eta = 0$ (or equivalently $J_1 = 0$), the $J_1 - J_2$ spin-1/2 nanotube model decomposes into two nearest-neighbor Heisenberg two-leg ladders of length L_y . This model has been studied extensively in the literature [47, 48, 50, 66, 67], and its ground state is well-known to be a resonating-valence-bond (RVB) state. The RVB state consists of a superposition of singlet coverings with nearest-neighbor singlets having larger weights. Nearest-neighbor singlets occur either along the leg or across the rungs of the ladder this phase is usually called “rung singlet” (RS) phase.

As we start from the RS state at $\eta = 0$ and gradually increase J_1 , the “red” and “blue” sublattices are reconnected, and we expect that singlets on J_1 bonds now become increasingly important, i.e. diagonal singlets and nearest-neighbor singlets along the chains. Since the gap remains open and the ground state remains singly degenerate, we remain in the RS phase for $\eta < \eta_{c,1}$. A similar behavior was reported, for example, in Ref. [53] that studies the properties of a model similar to ours (but without second-neighbor J_2 coupling along the chains) as

a function of leg to diagonal coupling.

In the other limit, $\eta \gg 1$, singlets on J_1 bonds are dominant. For $J_2 = 0$ the triplet sector of the nanotube model can be mapped onto the $S = 1$ Haldane model [52] and this limit thus corresponds to the Haldane phase [68–71]. This phase exhibits a fourfold degenerate ground state for OBC due to localized and protected spin-1/2 edge spin excitations. One can notice this degeneracy in Fig. 7(c) and 7(d) for $\eta \geq 0.65$ and $\eta \geq 0.93$, respectively. The Haldane phase is a well-known example of a nontrivial symmetry-protected topological (SPT) phase [70, 71]. SPTs are gapped phases with a symmetry protecting the topology of the state. In contrast, the RS phase is topologically trivial as it is adiabatically connected to a product state [71]. In order to determine the topology of the \mathbb{Z}_2 -helical phase, we investigate the degeneracy of the entanglement spectrum (ES) as a function of η in the next section.

C. Entanglement spectrum and string order parameters

In order to show that the two phases surrounding the \mathbb{Z}_2 -helical phase are indeed the topologically trivial RS and topologically nontrivial Haldane phases, we measure the entanglement spectrum for a cylinder of length $L_y = 128$ for the case $J_{2,x} = 2J_{2,y}$ and without pinning field ($\lambda = 0$). It has been shown that the lowest entanglement level for the RS and the Haldane phase are singly and doubly degenerate, respectively [70, 71]. In Fig. 8(a) one can notice the same degeneracy of the lowest level as expected for these two phases. The \mathbb{Z}_2 -helical phase displays degeneracies with the same parity as the RS phase, thus suggesting that it is not a nontrivial SPT phase.

Another way for characterizing the RS and Haldane phases is by measuring certain nonlocal string order parameters. We consider the same definition as given in Ref. [53] for the odd and even string order param-

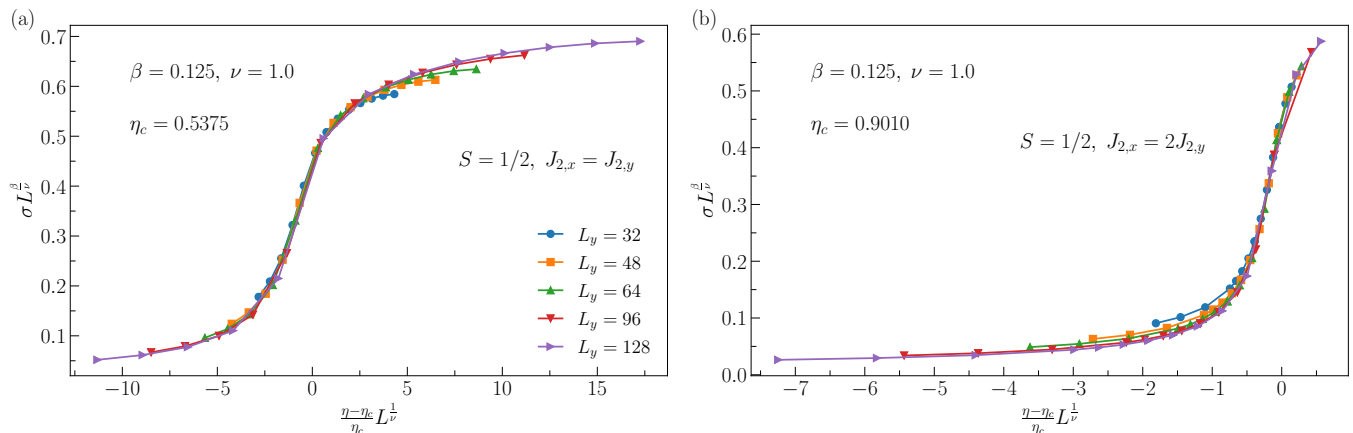


FIG. 9. Finite-size scaling data collapse of the \mathbb{Z}_2 -helical order parameter σ for (a) nanostrip $J_{2,x} = J_{2,y}$ and (b) nanotube $J_{2,x} = 2J_{2,y}$ geometries. The critical exponents are set to be those of the 2D Ising model universality class, i.e., $\beta = 1/8$ and $\nu = 1$. The location of the critical point $\eta_c \equiv \eta_{c,1}$ is set to the values shown in the figure.

ters: the former pairing nearest neighbors across rungs, whereas the latter pairs diagonal nearest neighbors. The notation of “even” and “odd” order parameteres arises from the parity of the number of singlet bonds that are broken if one horizontally cuts the chain. [53] In order to minimize boundary effects, we select pairs formed by sites $\ell = N/4$ and $N - \ell$, where $N = 4L_y$ is the total number of sites, as the starting and end points of the string order parameters, respectively. Therefore, given the site labelling in a snakelike pattern, the equations for the string order parameters are

$$\mathcal{O}_{\text{odd}}^z = - (S_\ell^z + S_{\ell-1}^z) \prod_{j=\ell+1}^{N-\ell-2} \exp(i\pi S_j^z) \times (S_{N-\ell}^z + S_{N-\ell-1}^z), \quad (16)$$

for the odd one, and

$$\mathcal{O}_{\text{even}}^z = - (S_\ell^z + S_{\ell+2}^z) e^{i\pi S_{\ell+1}^z} \prod_{j=\ell+3}^{N-\ell-1} \exp(i\pi S_j^z) \times (S_{N-\ell}^z + S_{N-\ell+2}^z), \quad (17)$$

for the even. Here and in the following, we assume L_y to be even. Hence, according to these definitions, $\mathcal{O}_{\text{odd}}^z \rightarrow 0$ if the ground state has predominantly rung singlets (RS phase), whereas $\mathcal{O}_{\text{even}}^z \rightarrow 0$ when the ground state has a majority of diagonal singlets (Haldane phase).

In Fig. 8(b) we show the two string order parameters, $\mathcal{O}_{\text{odd}}^z$ and $\mathcal{O}_{\text{even}}^z$, as a function of η for a nanotube of length $L_y = 128$. We focus on the nanotube case $J_{2,x} = 2J_{2,y}$, but we expect the result to be the same for the nanostrip. As we show in Appendix B, the data has already saturated for the chosen cylinder length L_y and these results are thus representative of the thermodynamic limit. Notice that $\mathcal{O}_{\text{odd}}^z \neq 0$ only in the Haldane phase, as expected. On the other hand, $\mathcal{O}_{\text{even}}^z$ remains finite within both the RS and the \mathbb{Z}_2 -helical phase. Its

value in the \mathbb{Z}_2 -helical phase is about four times less than the value of $\mathcal{O}_{\text{even}}^z$ at the RS phase.

D. Ising criticality

Finally, after having established the three different phases within the $J_1 - J_2$ nanotube model, let us return to the characterization of the critical point and the universality class of the transition at $\eta_{c,1}$. Using the results for the order parameter in the upper panels of Fig. 7, we perform a finite-size scaling analysis, which yields an estimate for the critical exponents β and ν . In Fig. 9 we show the outcome of the scaling analysis adopting the 2D Ising universality class critical parameters $\beta = 1/8$ and $\nu = 1$. We find a satisfactory collapse of the data points for both nanostrip and nanotube geometries.

One can obtain another critical exponent by directly evaluating the correlation function of the order parameter $\langle \sigma_i \sigma_j \rangle$. In order to reduce the effects of the open boundaries, we start from the plaquettes i and j in the middle of the cylinder and increase the separation between plaquette pairs by moving towards both ends of the nanotube. In Fig. 10 we show $\langle \sigma_i \sigma_j \rangle$ as a function of $|i - j|$ for a nanotube of length $L_y = 128$ and three different η values close to the critical point. Notice that we find an excellent agreement with the expected critical exponent value of the 2D Ising universality class for $\eta = 0.9015$, as shown by the power-law fitted dashed line.

Finally, we comment on the the cost of the DMRG simulations for the nanostrip versus the nanotube setups. We observed that the nanostrip case $J_{2,x} = J_{2,y}$ requires a significantly larger bond dimension than the nanotube case to achieve the same accuracy. For instance, for a cylinder of length $L_y = 64$ and choosing $\eta = 0.64$ and $\eta = 0.92$ for nanostrip and nanotube, respectively, inside the \mathbb{Z}_2 -helical phase near the first-order phase transition, the DMRG run for the nanostrip reaches the desired

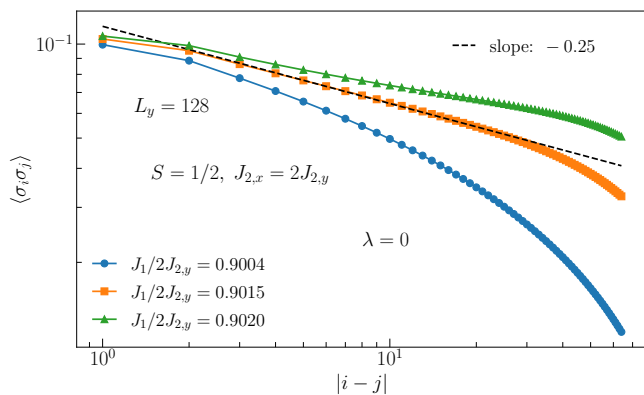


FIG. 10. Correlation function of the order parameter $\langle \sigma_i \sigma_j \rangle$ versus the separation between sites $|i - j|$ on a log-log scale for various $\eta = J_1/2J_2$ values. The data correspond to a cylinder of length $L_y = 128$ for the nanotube case $J_{2,x} = 2J_{2,y}$. The symmetry-breaking pinning field is set to zero, $\lambda = 0$. We find that the correlations decay algebraically with the expected 2D Ising exponent $\eta = 0.25$ for $J_1/(2J_{2,y}) = 0.9015$. The algebraic decay is observed up to a separation of about $|i-j| \approx 30$ when finite size effects set in. For $J_1/(2J_{2,y})$ smaller than the critical value, the correlations decay exponentially and they tend to saturate at a nonzero value for $J_1/(2J_{2,y}) > 0.9015$.

accuracy with a maximum bond dimension $m = 1322$, whereas it requires only $m = 414$ for the nanotube. This indicates that the ground state in the nanostrip case may be more complex and thus harder to converge to, which may deserve further studies.

V. DISCUSSION

In summary, both analytic and computational methods indicate that the \mathbb{Z}_2 nematic order of the two-dimensional $J_1 - J_2$ lattice model survives in the (1+1)-dimensional quantum limit of spin nanotubes. Furthermore the disordered states on either side of the \mathbb{Z}_2 ordered phase are distinct with different string order parameters, a feature that emerges already in the Schwinger boson treatment; from the two-dimensional perspective these distinct spin liquids were not anticipated, though they are qualitatively consistent with results for two-leg ladders, equivalent to our $N = 2$ spin nanotubes. We should note that we are not aware of any ladder calculations performed with the frustrated coupling profile that we present here so detailed comparison is not possible.

We have focused on gapped spin nanotubes with even N legs. The Schwinger Boson (SB) mean-field theory predicts two short-range spin liquid phases at small and large J_1/J_2 that are separated by an emergent \mathbb{Z}_2 helical phase for all values of S . This result is confirmed computationally for $S = 1/2$ $N_x = 2$ -leg ladders using Density Matrix Renormalization Group (DMRG). However the DMRG results indicate that the \mathbb{Z}_2 helical phase is

narrower than what was predicted by SB theory, though it is still present. There is however agreement between DMRG and SB that the \mathbb{Z}_2 helical phase is larger for $S = 1$ than it is for $S = 1/2$.

The \mathbb{Z}_2 helical phase is characterized by a local order parameter. Adopting the language of the ladder literature, it lies between rung singlet and Haldane spin liquid phases that are identified by distinct nonlocal even and odd string order parameters respectively. DMRG results indicate that neither of these string order parameters are present in the \mathbb{Z}_2 helical phase. This raised the interesting question of whether the phase with emergent local order is also topologically nontrivial in the sense of an SPT phase. We find that the entanglement spectrum displays no additional degeneracies and we thus conclude that the \mathbb{Z}_2 -helical phase is topologically trivial, just like the nearby RS phase. It interpolates between the RS and nontrivial SPT Haldane phase, which exhibits a twofold degenerate ES and an odd string order parameter that vanishes in the RS and \mathbb{Z}_2 -helical phase. We note that an even string order parameter with diagonal singlets was shown to be finite in the RS and the emergent \mathbb{Z}_2 phase, further indicating the similarity to the topologically trivial RS phase.

There are many questions that may motivate future research. First, we have here focused on gapped spin nanotubes with an even number N_x of spins along the short direction. Investigating half-integer spin chains with odd N_x , which are gapless, opens the possibility to explore the emergence of discrete symmetry breaking in models of algebraically correlated spins. Second, DMRG studies for higher spins $S > 1/2$ chains might explore the possible absence of the Haldane phase for integer spin. Third, the identification and scaling of the energy operator as well as other operators of the underlying conformal field theory [72] would confirm the 2D Ising nature of the quantum critical point. Similarly the scaling of the entanglement entropy with the bond dimension could be used to extract the central charge of the theory. Building a multi-scale entanglement renormalization ansatz (MERA) of the state at the quantum critical point would allow to further study this emergent phase transition driven by the condensation of a composite spin order parameter in more detail [73, 74]. Finally, these spin nanotube models could be studied using bosonization to rederive phase diagrams and to investigate the interplay of local order parameters, symmetry breaking and symmetry-protected topological order.

ACKNOWLEDGMENTS

This work was supported by DOE Basic Energy Sciences grant DE-SC0020353 (P.Ch and Z.Z.), NSF grant DMR-1830707 (P. Co) and by the U.S. Department of Energy (DOE), Office of Science, Basic Energy Sciences, Division of Materials Sciences and Engineering, including the grant of computer time at the National Energy Re-

search Scientific Computing Center (NERSC) in Berkeley, California (J.C.G. and P.P.O.). Part of the research (J.C.G. and P.P.O.) was performed at the Ames National Laboratory, which is operated for the U.S. DOE by Iowa State University under Contract DE-AC02-07CH11358. This work was supported by a Leverhulme Trust International Professorship grant number LIP-202-014 (S.L.S). For the purpose of Open Access, the author has applied a CC BY public copyright licence to any Author Accepted Manuscript version arising from this submission. P. Chandra thanks Princeton University for hospitality when this project was initiated.

Appendix A: Schwinger boson theory calculations

1. Mean-field equations

When $\eta \ll 1$ and S is large, one expects that there are two interpenetrating short-range-ordered antiferromagnetic sublattices, which are locked together and form a collinear state due to the order by disorder effect. In the collinear state, we take the translationally invariant mean-field ansatz shown in Fig. 2 (denoted as \mathbb{Z}_2 ansatz), which is consistent with the correlation of the corresponding state. When S decreases, the quantum fluctuation melts the collinear order and the two sublattices become decoupled. In this state, the expectation values Δ_+ and h_- should vanish simultaneously so that there is no correlation between the two decoupled antiferromagnetic sublattices (DAS) [56]. With this ansatz, the mean field Hamiltonian can be diagonalized by Fourier transform and Bogoliubov transformation.

For $N_x \geq 4$, the ground state energy per Kramers pair (or $N = 2$) per site is given by

$$\begin{aligned} \frac{E_{\mathbb{Z}_2}}{N_s} = & \frac{4}{J_1} \Delta_+^2 - \frac{4}{J_1} h_-^2 + \frac{4}{J_2} \Delta_x^2 + \frac{4}{J_2} \Delta_y^2 - \lambda(2S + 1) \\ & + \frac{1}{N_x} \sum_{k_x} \int_{-2\pi}^{2\pi} \frac{dk_y}{4\pi} \omega_{\mathbb{Z}_2}(k_x, k_y), \end{aligned} \quad (\text{A1})$$

where the bosonic spectrum reads

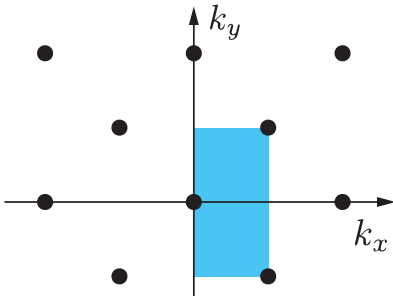
$$\omega_{\mathbb{Z}_2} = \sqrt{s^2 - t^2}, \quad (\text{A2})$$

and

$$s = \lambda + 2h_- \cos \frac{k_x - k_y}{2}, \quad (\text{A3})$$

$$t = 2 \left(\sin \frac{k_x + k_y}{2} \Delta_+ + \sin k_x \Delta_x + \sin k_y \Delta_y \right). \quad (\text{A4})$$

For $N_x = 2$ case, the J_2 associated with Δ_y (Δ_x) in Eq. (A1) should be replaced by $J_{2,y}$ ($J_{2,x}/2$) while the rest of the equation remains unchanged (see our definition in Sec. IV). In the below, we only show equations derived



for $N_x = 4$ case and their modification for $N_x = 2$ are straightforward. For convenience we have set lattice constant $a = 1$ (see Fig. 2) and choose the Brillouin zone to be $0 \leq k_x < 2\pi, -2\pi \leq k_y < 2\pi$ (see Fig. 11). As will be discussed later, in the \mathbb{Z}_2 ansatz k_x takes discrete value $k_x = 2\pi m/N_x + \pi/2$, where $m = 0, 1, \dots, N_x - 1$. By minimizing the ground state energy one obtains the set of mean field equations:

$$2S + 1 = \frac{1}{N_x} \sum_{k_x} \int_{-2\pi}^{2\pi} \frac{dk_y}{4\pi} \frac{s}{\omega_{\mathbb{Z}_2}}, \quad (\text{A5})$$

$$\frac{4}{J_1} h_- = \frac{1}{N_x} \sum_{k_x} \int_{-2\pi}^{2\pi} \frac{dk_y}{4\pi} \frac{s}{\omega_{\mathbb{Z}_2}} \cos \frac{k_x - k_y}{2}, \quad (\text{A6})$$

$$\frac{4}{J_1} \Delta_+ = \frac{1}{N_x} \sum_{k_x} \int_{-2\pi}^{2\pi} \frac{dk_y}{4\pi} \frac{t}{\omega_{\mathbb{Z}_2}} \sin \frac{k_x + k_y}{2}, \quad (\text{A7})$$

$$\frac{4}{J_2} \Delta_x = \frac{1}{N_x} \sum_{k_x} \int_{-2\pi}^{2\pi} \frac{dk_y}{4\pi} \frac{t}{\omega_{\mathbb{Z}_2}} \sin k_x, \quad (\text{A8})$$

$$\frac{4}{J_2} \Delta_y = \frac{1}{N_x} \sum_{k_x} \int_{-2\pi}^{2\pi} \frac{dk_y}{4\pi} \frac{t}{\omega_{\mathbb{Z}_2}} \sin k_y. \quad (\text{A9})$$

To determine whether a continuous phase transition occurs, we also need the Hessian matrix elements $Q = \partial^2 E_{\mathbb{Z}_2} / (N_s \partial \alpha_i \partial \alpha_j)$, where

$$\alpha = (\lambda, \Delta_x, \Delta_y, h_-, \Delta_+) \quad (\text{A10})$$

is the shorthand for the mean-field parameters. It turns out that when $h_- = \Delta_+ = 0$ the 5×5 Hessian matrix Q is block diagonal

$$Q = \begin{pmatrix} X & 0 \\ 0 & Y \end{pmatrix} \quad (\text{A11})$$

where

$$X = \begin{pmatrix} -\int_k \frac{t^2}{\omega^3} & 2 \int_k \frac{\sin k_x st}{\omega^3} & 2 \int_k \frac{\sin k_y st}{\omega^3} \\ 2 \int_k \frac{\sin k_x st}{\omega^3} & \frac{8}{J_2} - 4 \int_k \frac{\sin^2 k_x s^2}{\omega^3} & -4 \int_k \frac{\sin k_x \sin k_y s^2}{\omega^3} \\ 2 \int_k \frac{\sin k_y st}{\omega^3} & -4 \int_k \frac{\sin k_x \sin k_y s^2}{\omega^3} & \frac{8}{J_2} - 4 \int_k \frac{\sin^2 k_y s^2}{\omega^3} \end{pmatrix}, \quad (\text{A12})$$

$$Y = \begin{pmatrix} -\frac{8}{J_1} - 4 \int_k \frac{\cos^2 \frac{k_x - k_y}{2} t^2}{\omega^3} & 4 \int_k \frac{\cos \frac{k_x - k_y}{2} \sin \frac{k_x + k_y}{2} st}{\omega^3} \\ 4 \int_k \frac{\cos \frac{k_x - k_y}{2} \sin \frac{k_x + k_y}{2} st}{\omega^3} & \frac{8}{J_1} - 4 \int_k \frac{\sin^2 \frac{k_x + k_y}{2} s^2}{\omega^3} \end{pmatrix} \quad (\text{A13})$$

and we have used shorthand $\int_k \equiv \frac{1}{N_x} \sum_{k_x} \int_{-2\pi}^{2\pi} \frac{dk_y}{4\pi}$, $\omega \equiv \omega_{\mathbb{Z}_2}$.

When $\eta \gg 1$, the system is expected to have Néel short range order (SRO). In the symplectic-N Schwinger boson theory, we consider the mean-field ansatz (Néel ansatz) shown in Fig. 2. The ground state energy per site can be shown to be

$$\begin{aligned} \frac{E_N}{N_s} &= \frac{4}{J_1} \Delta_+^2 + \frac{4}{J_1} \Delta_-^2 - \frac{4}{J_2} h_x^2 - \frac{4}{J_2} h_y^2 - \lambda(2S + 1) \\ &+ \frac{1}{N_x} \sum_{k_x} \int_{-2\pi}^{2\pi} \frac{dk_y}{4\pi} \omega_N(k_x, k_y), \end{aligned} \quad (\text{A14})$$

where k_x takes discrete values $k_x = 2\pi m/N_x$, $m = 0, 1, \dots, N_x - 1$. The bosonic spectrum is

$$\omega_N = \sqrt{u^2 - v^2}, \quad (\text{A15})$$

where

$$u = \lambda + 2h_x \cos k_x + 2h_y \cos k_y, \quad (\text{A16})$$

and

$$v = 2 \sin \frac{k_x - k_y}{2} \Delta_- - 2 \sin \frac{k_x + k_y}{2} \Delta_+. \quad (\text{A17})$$

The self-consistent mean-field equations are

$$2S + 1 = \frac{1}{N_x} \sum_{k_x} \int_{-2\pi}^{2\pi} \frac{dk_y}{4\pi} \frac{u}{\omega_N}, \quad (\text{A18})$$

$$\frac{4}{J_1} \Delta_- = \frac{1}{N_x} \sum_{k_x} \int_{-2\pi}^{2\pi} \frac{dk_y}{4\pi} \frac{v}{\omega_N} \sin \frac{k_x - k_y}{2}, \quad (\text{A19})$$

$$\frac{4}{J_1} \Delta_+ = -\frac{1}{N_x} \sum_{k_x} \int_{-2\pi}^{2\pi} \frac{dk_y}{4\pi} \frac{v}{\omega_N} \sin \frac{k_x + k_y}{2}, \quad (\text{A20})$$

$$\frac{4}{J_2} h_x = \frac{1}{N_x} \sum_{k_x} \int_{-2\pi}^{2\pi} \frac{dk_y}{4\pi} \frac{u}{\omega_N} \cos k_x, \quad (\text{A21})$$

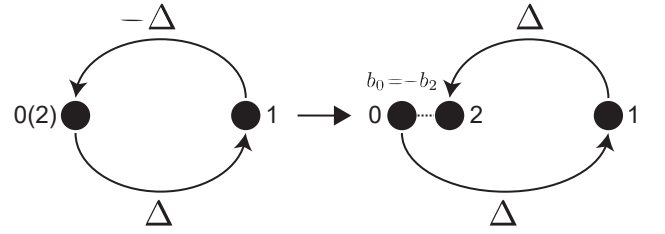


FIG. 12. The mean-field ansatz of a two-site Heisenberg model. Left: Boson wavefunction is periodic and the mean-field ansatz is not translationally invariant along the loop. Right: Wavefunction is anti-periodic but the ansatz has translational symmetry.

$$\frac{4}{J_2} h_y = \frac{1}{N_x} \sum_{k_x} \int_{-2\pi}^{2\pi} \frac{dk_y}{4\pi} \frac{u}{\omega_N} \cos k_y. \quad (\text{A22})$$

By solving the above equations self-consistently and comparing the energies Eqs. (A1) and (A14), one can determine the first-order phase transition lines shown in the main text figures.

2. \mathbb{Z}_2 phase transition

In this section, we use Schwinger boson theory to analytically investigate the \mathbb{Z}_2 phase transition of spin nanotube when $\eta \ll 1$.

a. $N_x = 2$ case

We first consider the case (ii) $J_{2,x} = 2J_{2,y} = 2J$, for which we refer as the spin nanotube. In the $N_x = 2$ case, the bosons have anti-periodic instead of periodic boundary condition along the x -direction, so k_x takes value $\frac{\pi}{2}, \frac{3\pi}{2}$. To see this, one can consider a simpler case: a two-site antiferromagnetic model on a ring shown in Fig. 12. Because $\Delta_{12} = -\Delta_{21}$, to make the bosonic Hamiltonian translationally invariant with constant Δ around the

ring, one has to apply a singular gauge transformation leaving Δ_{10}, b_0, b_1 invariant but $b_2 \rightarrow -b_2, \Delta_{12} \rightarrow -\Delta_{12}$, which makes the wavefunction anti-periodic. When $h_- = \Delta_+ = 0$ Eqs. (A5)-(A9) can be simplified to

$$2S + 1 = \int_{-\pi}^{\pi} \frac{dk'_y}{2\pi} \frac{1}{\sqrt{1-z^2}}, \quad (\text{A23})$$

$$\frac{4}{J_2} \Delta_x = \int_{-\pi}^{\pi} \frac{dk'_y}{2\pi} \frac{z}{\sqrt{1-z^2}}, \quad (\text{A24})$$

$$\frac{4}{J_2} \Delta_y = \int_{-\pi}^{\pi} \frac{dk'_y}{2\pi} \frac{z \cos k'_y}{\sqrt{1-z^2}}, \quad (\text{A25})$$

where for convenience we have made substitution $k_y \rightarrow k'_y + \frac{\pi}{2}$ and $z = 2(\Delta_x + \cos k_y \Delta_y)/\lambda$.

When S is small, the only two non-zero mean-field parameters are λ, Δ_x or λ, Δ_y , and we verify that the former one is energetically favorable. Solving Eq.(A23) and Eq. (A24) one obtains

$$\lambda = J_2(S + \frac{1}{2}), \quad \Delta_x = \frac{J_2 \sqrt{S(S+1)}}{2}, \quad (\text{A26})$$

which means at small S , the ground state is a valence bond solid in which every two sites connected by the J_2 bond in the x -direction form singlets. This is because we are considering the case $J_{2,x} = 2J_{2,y}$ where the J_2 coupling along the x -direction is doubled and is twice as large as the one along the y -direction, so singlet state is favored due to large quantum fluctuation. When S further increases and approaches a lower critical value S_{cl} , the system becomes unstable to being antiferromagnetically short-range ordered, and Δ_y acquires a non-vanishing value. To see this, one could evaluate the Hessian matrix element $\frac{\partial^2 E_g}{\partial \alpha_3^2}$ (note that when $\Delta_y = h_- = \Delta_+ = 0$ the Hessian matrix elements $\frac{\partial^2 E_g}{\partial \alpha_3 \partial \alpha_j}$ all vanish for $j \neq 3$), which vanishes at the transition point

$$\frac{8}{J_2} - 4 \int_k \frac{\sin^2 k_y s^2}{\omega_{Z_2}^3} = 0. \quad (\text{A27})$$

With Eq.(A26), one obtains $S_{cl} = 1/\sqrt{2} - 1/2 \approx 0.21$.

As S further increases, if J_1 coupling is absent, $\lambda, \Delta_x, \Delta_y$ all increase and at large S approaches $\Delta_x/\lambda \sim \Delta_y/\lambda \sim 1/4$. In this regime it is useful to define a small parameter $\epsilon = 1 - 2\frac{\Delta_x + \Delta_y}{\lambda}$ and $z = (1-\epsilon) \cos^2 \frac{k'_y}{2} + O(\frac{1}{\ln \epsilon})$ when $\epsilon \ll 1$. From Eqs. (A23)(A24) and (A25) one obtains

$$2S + 1 \approx \frac{1}{\sqrt{2\pi}} [5 \ln 2 - \ln \epsilon], \quad \lambda \approx -\frac{J_2}{\sqrt{2\pi}} \ln \epsilon. \quad (\text{A28})$$

Note there are four degenerate quasi-gapless modes at $\mathbf{k} = (\pi/2, \pi/2), (\pi/2, -3\pi/2), (3\pi/2, 3\pi/2), (3\pi/2, -\pi/2)$ with corresponding correlation length $\xi \sim 1/\sqrt{\epsilon}$, which

are reminiscent of the Goldstone modes of two uncoupled antiferromagnets. When J_1 is present, at some point the system is unstable to the collinear order and Δ_+, h_- develops, which hybridizes the four degenerate quasi-gapless modes and gives rise to only two quasi-gapless modes. At the transition point, the determinant of the Hessian in the (h_-, Δ_+) sector

$$\det(Y) = (A_1 + A_2 + 2B)(A_1 + A_2 - 2B) - \left(A_1 - A_2 - \frac{8}{J_1}\right)^2, \quad (\text{A29})$$

should vanish. In the above equation we define $A_1 = -2 \int_k (\cos^2 \frac{k_x - k_y}{2} t^2)/\omega^3$, $A_2 = -2 \int_k (\sin^2 \frac{k_x + k_y}{2} s^2)/\omega^3$ and $B = 2 \int_k (\cos \frac{k_x - k_y}{2} \sin \frac{k_x + k_y}{2} st)/\omega^3$. One can show that $|A_1|, |A_2|, |B|$ are identical to all divergent orders, and the lowest order contribution is given by

$$A_1 \sim A_2 \sim -B \approx \frac{2}{J_2 \epsilon \ln \epsilon}. \quad (\text{A30})$$

Nevertheless, their differences are convergent in the limit $\epsilon \rightarrow 0$ and particularly,

$$A_1 + A_2 + 2B = \frac{1}{2\pi\lambda} \int_{-\pi}^{\pi} dk'_y \frac{(z-1)(1+\cos k'_y)}{(z+1)\sqrt{1-z^2}} = -\frac{\gamma_2}{2\sqrt{2}\pi\lambda} \approx \frac{\gamma_2}{2J_2 \ln \epsilon}, \quad (\text{A31})$$

$$A_1 - A_2 = \frac{1}{2\pi\lambda} \int_{-\pi}^{\pi} dk'_y \frac{1 + \cos k'_y}{\sqrt{1-z^2}} \approx -\frac{\sqrt{2} \ln \epsilon}{\pi\lambda} \approx \frac{2}{J_2} \quad (\text{A32})$$

where $\gamma_2 = 8(\sqrt{2} \ln(\sqrt{2} + 1) - 1) \approx 1.97$. Insert Eq. (A31) and Eq. (A32) to Eq. (A29) one finds, to the lowest order, the determinant of Hessian vanishes when

$$\sqrt{\epsilon} \ln \epsilon = \frac{\sqrt{\gamma}}{(1 - \frac{2}{\eta})}. \quad (\text{A33})$$

At large S and small η , the critical spin S_{ch} is hence given by Eq. (11) in the main text.

For the $J_{2,x} = J_{2,y}$ case (denoted as the spin nanostrip), one could find that its phase diagram is similar to the spin nanotube case, except for the absence of valence bond solid (VBS) phase. The vanishing VBS phase can be understood by noting that, for general $J_{2,x} \geq J_{2,y}$, Δ_y becomes nonzero when $S \geq S_{cl} = (\sqrt{J_{2,x}/J_{2,y}} - 1)/2$, and when $J_{2,x} = J_{2,y}$ S_{cl} is exactly zero. Through a similar calculation used to compute the $J_{2,x} = 2J_{2,y}$ case, one obtains Eq. (10) in the main text, and the derivation is not shown here.

b. $N_x \geq 4$ case

For general N_x one can numerically confirm that when $N_x \bmod 4 = 0$ the lowest energy bosonic state is the one

with periodic boundary condition (or translationally invariant ansatz), while if $N_x \bmod 4 = 2$, the lowest energy state corresponds to the one with anti-periodic boundary condition (or ansatz that lacks translational symmetry). Therefore k_x takes value $\frac{2\pi}{N_x}m + \frac{\pi}{2}$, consistent with the special case $N_x = 2$. This periodic boundary condition indicates that system can lower its energy by having those quasi-gapless subbands at transverse momentum $k_x = \pi/2, 3\pi/2$. Similar to the $N_x = 2$ case, one could first find the critical spin S_{cl} where Δ_y develops and then look for the critical spin S_{ch} where \mathbb{Z}_2 phase transition occurs. However, for $N_x \geq 4$, it turns out that Δ_x and Δ_y are both present for any finite S if η is small, as a consequence of that J_2 along x -direction is no longer doubled. To see this, one can set $S = 0^+$, solve the mean field equations (A5)-(A9) and obtain

$$\lambda_0 = \lim_{S \rightarrow 0} \lambda = \frac{J_2}{2N_x} \sum_{k_x} \sin^2 k_x = \begin{cases} J_2/2, & N_x = 2 \\ J_2/4, & N_x \geq 4 \end{cases}. \quad (\text{A34})$$

The Hessian at $S = 0^+$ is diagonal and given by

$$\frac{1}{N_s} \frac{\partial^2 E_g}{\partial \alpha_i \alpha_j} = \begin{pmatrix} 0 & & & \\ & 0 & & \\ & \frac{8}{J_2} - \frac{2}{\lambda_0} & & \\ & & -\frac{8}{J_1} & \\ & & & \frac{8}{J_1} - \frac{2}{\lambda_0} \end{pmatrix}_{ij}. \quad (\text{A35})$$

Thus for $N_x \geq 4$, $\frac{\partial^2 E_g}{\partial \alpha_2^2} = \frac{\partial^2 E_g}{\partial \alpha_3^2} = 0$ when $S = 0$, which indicates that Δ_x and Δ_y acquire expectation value simultaneously at infinitesimal S when $\eta < 1/2$. When $\eta > 1/2$, note that $\frac{\partial^2 E_g}{\partial \alpha_5^2}$ becomes negative, indicating that Δ_+ will first develop while other mean-field parameters except λ remain zero at small S . We denote this phase as the decoupled antiferromagnetic chains (DAC) and show it in Fig. 3.

For our purpose we focus on the $\eta < 1/2$ case and solve for the critical spin S_{ch} where \mathbb{Z}_2 order phase transition occurs. When η is close to $1/2$, the \mathbb{Z}_2 phase transition is expected to occur at small S where the bosonic gap is large compared to $1/N_x$. In the other words, the phase transition occurs when the Heisenberg correlation length ξ is much smaller than the width N_x of the nanotube, which corresponds to the two dimensional limit. In this case, all the sums over k_x can be converted to integrals as functions such as $1/\omega$ are smooth, which is equivalent to setting $N_x = \infty$. The critical S_{ch} can be solved numerically by letting the determinant of Hessian Eq. (A13) be zero and the result is shown as the red dotted line in Fig. (3).

At small $\eta \approx 0$, the \mathbb{Z}_2 phase transition occurs at large S as in the $N_x = 2$ case, corresponding to the one dimensional limit as $\xi \gg N_x$. The mean field equations are similar to the $N_x = 2$ case, except that there are also contributions from gapped subbands:

$$2S + 1 = \frac{1}{N_x} \left[2 \int_{-\pi}^{\pi} \frac{dk'_y}{2\pi} \frac{1}{\sqrt{1-z^2}} + I_S \right], \quad (\text{A36})$$

$$\frac{4}{J_2} \Delta_x = \frac{1}{N_x} \left[2 \int_{-\pi}^{\pi} \frac{dk'_y}{2\pi} \frac{u}{\sqrt{1-z^2}} + I_x \right], \quad (\text{A37})$$

$$\frac{4}{J_2} \Delta_y = \frac{1}{N_x} \left[2 \int_{-\pi}^{\pi} \frac{dk'_y}{2\pi} \frac{u \cos k'_y}{\sqrt{1-z^2}} + I_y \right], \quad (\text{A38})$$

where at large S

$$I_s \approx \sum_{k'_x \neq 0, \pi} \int_{-\pi}^{\pi} \frac{dk'_y}{2\pi} \frac{1}{\sqrt{1-\tilde{z}^2}}, \quad (\text{A39})$$

$$I_x \approx \sum_{k'_x \neq 0, \pi} \int_{-\pi}^{\pi} \frac{dk'_y}{2\pi} \frac{\tilde{u} \cos k_x}{\sqrt{1-\tilde{z}^2}}, \quad (\text{A40})$$

$$I_y \approx \sum_{k'_x \neq 0, \pi} \int_{-\pi}^{\pi} \frac{dk'_y}{2\pi} \frac{\tilde{u} \cos k'_y}{\sqrt{1-\tilde{z}^2}}, \quad (\text{A41})$$

where we define $k'_x = k_x - \pi/2$ and $\tilde{z} = (\cos k'_x + \cos k'_y)/2$. Combine the above equations one obtains

$$2S + 1 \approx \frac{1}{N_x \pi} [\sqrt{2}(5 \ln 2 - \ln \epsilon) + \pi I_S], \quad (\text{A42})$$

$$\lambda \approx -\frac{\sqrt{2} J_2}{N_x \pi} \ln \epsilon.$$

The determinant of the Hessian can be determined in a manner similar to the $N_x = 2$ case:

$$A_1 + A_2 - 2B \approx \frac{8}{J_2 \epsilon \ln \epsilon}, \quad (\text{A43})$$

$$A_1 - A_2 \approx \frac{2}{J_2}, \quad (\text{A44})$$

and

$$A_1 + A_2 + 2B \quad (\text{A45})$$

$$= -\frac{1}{N_x} \left[\frac{2}{\lambda} \int_{-\pi}^{\pi} \frac{dk'_y}{2\pi} \frac{(1-u)(1+\cos k'_y)}{(u+1)\sqrt{1-u^2}} + \frac{2I_-}{\lambda} \right]$$

$$= -2 \frac{\gamma/2\sqrt{2}\pi + I_-}{N_x \lambda},$$

where

$$I_- \approx \sum_{k'_x \neq 0, \pi} \int_{-\pi}^{\pi} \frac{dk_y}{2\pi} \frac{(1-\tilde{u})(1+\cos k'_y)}{2(\tilde{u}+1)\sqrt{1-\tilde{u}^2}}. \quad (\text{A46})$$

Combine all the above equations with Eq. (A29) one obtains

$$S_{\text{ch}} \exp\left(-\frac{N_x \pi (S_{\text{ch}} + 1/2)}{\sqrt{2}}\right)$$

$$= \exp\left(-\frac{\pi}{2\sqrt{2}} I_S\right) \frac{\sqrt{\gamma + 2\sqrt{2}\pi I_-}}{16 N_x \pi} \eta. \quad (\text{A47})$$

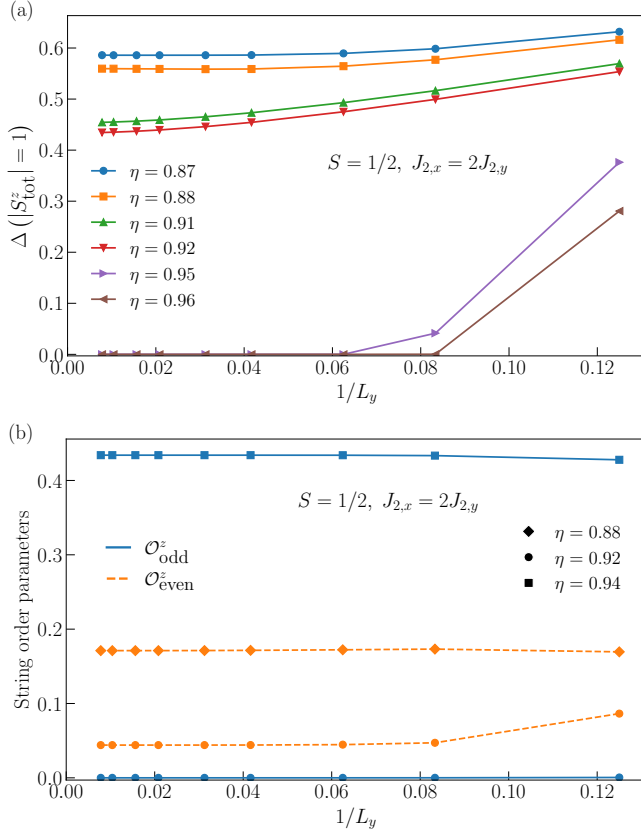


FIG. 13. (a) Scaling of the spin gap $\Delta(|S_{\text{tot}}^z|=1)$ and (b) the string order parameters $\mathcal{O}_{\text{odd}}^z$ and $\mathcal{O}_{\text{even}}^z$ (lower panel) with the nanotube length L_y for several values of $\eta = J_1/2J_2$. The data corresponds to the case where $J_{2,x} = 2J_{2,y}$.

Appendix B: Scaling of the spin gap and string order parameters

For the sake of completeness, we show here a few examples of the scaling of the spin gap and string order parameters with respect to the system size. In Fig. 13(a) we have selected several $\eta = J_1/2J_2$ values, in order to cover all three phases, to present the scaling of the spin gap $\Delta(|S_{\text{tot}}^z|=1)$ as a function of the inverse of the nanotube length L_y . Here we have focused only on the nanotube setup, as we are able to reach larger system sizes than the nanostrip case. Moreover, we should point out that the scaling plot for the energy gap between the first-excited and ground states of sector $S_{\text{tot}}^z = 0$ does not behave as smoothly as the spin gap represented in Fig. 13(a). The reason lies in a poor choice of the weight factor w of the penalized Hamiltonian, which we have set in our preliminary calculations as $w = 10$ regardless of system size and η value. However, by tuning the parameter w , and also by adding noise to the initial sweeps of the DMRG method, we have verified that one can obtain more consistent results for the energy gap.

Similarly, Fig. 13(b) displays the scaling of the string order parameters $\mathcal{O}_{\text{odd}}^z$ and $\mathcal{O}_{\text{even}}^z$ (Eqs. 16 and 17, respectively). For each string order parameter, we have chosen two η values, one within the \mathbb{Z}_2 -helical phase and the other within the phase where the corresponding parameter is finite. Notice that the string order parameters saturate for relatively small system sizes, thus indicating that the data for the largest system, namely $L_y = 128$, is a good approximation to the thermodynamic limit.

-
- [1] J. Villain, *J. Phys. France* **38**, 385 (1977).
[2] J. Villain, R. Bidaux, J.-P. Carton, and R. Conte, *J. Phys. France* **41**, 1263 (1980).
[3] E. Shender, *Soviet Journal of Experimental and Theoretical Physics* **56**, 178 (1982).
[4] R. Moessner, *Can. J. Phys.* **79**, 1283 (2001).
[5] P. Chandra, P. Coleman, and A. I. Larkin, *Phys. Rev. Lett.* **64**, 88 (1990).
[6] C. L. Henley and N.-g. Zhang, *Phys. Rev. Lett.* **81**, 5221 (1998).
[7] C. Weber, L. Capriotti, G. Misguich, F. Becca, M. Elhadj, and F. Mila, *Phys. Rev. Lett.* **91**, 177202 (2003).
[8] A. Mulder, R. Ganesh, L. Capriotti, and A. Paramekanti, *Phys. Rev. B* **81**, 214419 (2010).
[9] M. E. Zhitomirsky, M. V. Gvozdkova, P. C. W. Holdsworth, and R. Moessner, *Phys. Rev. Lett.* **109**, 077204 (2012).
[10] L. Savary, K. A. Ross, B. D. Gaulin, J. P. C. Ruff, and L. Balents, *Phys. Rev. Lett.* **109**, 167201 (2012).
[11] G.-W. Chern and R. Moessner, *Phys. Rev. Lett.* **110**, 077201 (2013).
[12] A.-M. Nedić, V. L. Quito, Y. Sizyuk, and P. P. Orth, *Three-state Potts nematic order in stacked frustrated spin models with SO(3) symmetry* (2022), [arxiv:arXiv:2210.04900](https://arxiv.org/abs/2210.04900).
[13] J. Strockoz, D. S. Antonenko, D. LaBelle, and J. W. F. Venderbos, *Excitonic instability towards a Potts-nematic quantum paramagnet* (2022), [arxiv:arXiv:2211.11739](https://arxiv.org/abs/2211.11739).
[14] P. Orth, P. Chandra, P. Coleman, and J. Schmalian, *Phys. Rev. Lett.* **109**, 237205 (2012).
[15] P. Orth, P. Chandra, P. Coleman, and J. Schmalian, *Phys. Rev. B* **89**, 094417 (2014).
[16] B. Jeevanesan, P. Chandra, P. Coleman, and P. P. Orth, *Physical Review Letters* **115**, 177201 (2015).
[17] R. M. Fernandes, P. P. Orth, and J. Schmalian, *Annual Review of Condensed Matter Physics* **10**, 133 (2019).
[18] R. Moessner and S. L. Sondhi, *Phys. Rev. B* **63**, 224401 (2001).
[19] R. Moessner, S. L. Sondhi, and P. Chandra, *Phys. Rev. B* **64**, 144416 (2001).
[20] S. Wessel and M. Troyer, *Phys. Rev. Lett.* **95**, 127205 (2005).
[21] M. Boninsegni and N. Prokof'ev, *Phys. Rev. Lett.* **95**, 237204 (2005).
[22] R. G. Melko, A. Paramekanti, A. A. Burkov, A. Vishwanath, D. N. Sheng, and L. Balents, *Phys. Rev. Lett.* **95**, 127207 (2005).
[23] D. Heidarian and K. Damle, *Phys. Rev. Lett.* **95**, 127206

- (2005).
- [24] T.-C. Hsieh, H. Ma, and L. Radzihovsky, *Phys. Rev. A* **106**, 023321 (2022).
- [25] A. G. Green, G. Conduit, and F. Krüger, *Annual Review of Condensed Matter Physics* **9**, 59 (2018).
- [26] O. Gauthé and F. Mila, *Phys. Rev. Lett.* **128**, 227202 (2022).
- [27] R. R. P. Singh, W. Zheng, J. Oitmaa, O. P. Sushkov, and C. J. Hamer, *Phys. Rev. Lett.* **91**, 017201 (2003).
- [28] G. Misguich, B. Bernu, and L. Pierre, *Phys. Rev. B* **68**, 113409 (2003).
- [29] H. Li and T. Li, *Phys. Rev. B* **106**, 035112 (2022).
- [30] C. Xu, M. Müller, and S. Sachdev, *Phys. Rev. B* **78**, 020501 (2008).
- [31] R. M. Fernandes, A. V. Chubukov, J. Knolle, I. Eremin, and J. Schmalian, *Phys. Rev. B* **85**, 024534 (2012).
- [32] Q. Si, R. Yu, and E. Abrahams, *Nature Reviews Materials* **601**, 35 (2022).
- [33] R. Fernandes, A. Coldea, H. Ding, I. Fisher, P. Hirschfeld, and G. Kotliar, *Nature* **601**, 35 (2022).
- [34] S. Gopalakrishnan, Y. E. Shchadilova, and E. Demler, *Phys. Rev. A* **96**, 063828 (2017).
- [35] M. Hecker and J. Schmalian, ArXiv e-prints 1712.07523 (2017), [arxiv:1712.07523](https://arxiv.org/abs/1712.07523).
- [36] L. Nie, A. V. Maharaj, E. Fradkin, and S. A. Kivelson, *Phys. Rev. B* **96**, 085142 (2017).
- [37] J. Schnack, H. Nojiri, P. Kögerler, G. J. T. Cooper, and L. Cronin, *Phys. Rev. B* **70**, 174420 (2004).
- [38] V. O. Garlea, A. Zheludev, L.-P. Regnault, J.-H. Chung, Y. Qiu, M. Boehm, K. Habicht, and M. Meissner, *Phys. Rev. Lett.* **100**, 037206 (2008).
- [39] A. Zheludev, V. O. Garlea, L.-P. Regnault, H. Manaka, A. Tsvelik, and J.-H. Chung, *Phys. Rev. Lett.* **100**, 157204 (2008).
- [40] V. O. Garlea, A. Zheludev, K. Habicht, M. Meissner, B. Grenier, L.-P. Regnault, and E. Ressouche, *Phys. Rev. B* **79**, 060404 (2009).
- [41] T. Sakai, M. Sato, K. Okamoto, K. Okunishi, and I. Chigak, *J. Phys: Cond. Mat.* **22**, 403201 (2022).
- [42] M. Arlego, W. Brenig, Y. Rahnavard, B. Willenberg, H. D. Rosales, and G. Rossini, *Phys. Rev. B* **87**, 014412 (2013).
- [43] Y. Fuji, S. Nishimoto, H. Nakada, and M. Oshikawa, *Phys. Rev. B* **89**, 054425 (2014).
- [44] X. Plat, Y. Fuji, S. Capponi, and P. Pujol, *Phys. Rev. B* **91**, 064411 (2015).
- [45] C. Lamas, D. Cabra, P. Pujol, and G. Rossini, *Eur. Phys. J. B* **88**, 176 (2015).
- [46] T. Ito, C. Iino, and N. Shibata, *Phys. Rev. B* **97**, 184409 (2018).
- [47] E. Dagotto, J. Riera, and D. Scalapino, *Phys. Rev. B* **45**, 5744 (1992).
- [48] T. Barnes, E. Dagotto, J. Riera, and E. S. Swanson, *Phys. Rev. B* **47**, 3196 (1993).
- [49] S. Gopalan, T. M. Rice, and M. Sgrist, *Phys. Rev. B* **49**, 8901 (1994).
- [50] S. R. White, R. M. Noack, and D. J. Scalapino, *Phys. Rev. Lett.* **73**, 886 (1994).
- [51] M. Troyer, H. Tsunetsugu, and D. Würtz, *Phys. Rev. B* **50**, 13515 (1994).
- [52] E. H. Kim, G. Fáth, J. Sólyom, and D. J. Scalapino, *Phys. Rev. B* **62**, 14965 (2000).
- [53] G. Fáth, O. Legeza, and J. Sólyom, *Phys. Rev. B* **63**, 134403 (2001).
- [54] E. H. Kim, O. Legeza, and J. Sólyom, *Phys. Rev. B* **77**, 205121 (2008).
- [55] O. A. Starykh and L. Balents, *Phys. Rev. Lett.* **93**, 127202 (2004).
- [56] R. Flint and P. Coleman, *Phys. Rev. B* **79**, 014424 (2009).
- [57] S. R. White, *Phys. Rev. Lett.* **69**, 2863 (1992).
- [58] U. Schollwöck, *Annals of Physics* **326**, 96 (2011).
- [59] E. Stoudenmire and S. R. White, *Annual Review of Condensed Matter Physics* **3**, 111 (2012).
- [60] M. Fishman, S. R. White, and E. M. Stoudenmire, *SciPost Phys. Codebases*, 4 (2022).
- [61] C. L. Henley, *Phys. Rev. Lett.* **62**, 2056 (1989).
- [62] A. Auerbach, *Interacting Electrons and Quantum Magnetism* (Springer Science & Business Media, 2012).
- [63] D. P. Arovas and A. Auerbach, *Phys. Rev. B* **38**, 316 (1988).
- [64] N. Read and S. Sachdev, *Phys. Rev. Lett.* **66**, 1773 (1991).
- [65] M. Fishman, S. R. White, and E. M. Stoudenmire, *SciPost Phys. Codebases*, 4 (2022).
- [66] D. G. Shelton, A. A. Nersesyan, and A. M. Tsvelik, *Phys. Rev. B* **53**, 8521 (1996).
- [67] D. C. Cabra, A. Honecker, and P. Pujol, *Phys. Rev. Lett.* **79**, 5126 (1997).
- [68] F. D. M. Haldane, *Phys. Rev. Lett.* **50**, 1153 (1983).
- [69] I. Affleck, T. Kennedy, E. H. Lieb, and H. Tasaki, *Phys. Rev. Lett.* **59**, 799 (1987).
- [70] F. Pollmann, A. M. Turner, E. Berg, and M. Oshikawa, *Phys. Rev. B* **81**, 064439 (2010).
- [71] F. Pollmann, E. Berg, A. M. Turner, and M. Oshikawa, *Phys. Rev. B* **85**, 075125 (2012).
- [72] Y. Zou, A. Milsted, and G. Vidal, *Phys. Rev. Lett.* **124**, 040604 (2020).
- [73] G. Vidal, *Phys. Rev. Lett.* **99**, 220405 (2007).
- [74] J. Argüello-Luengo, A. Milsted, and G. Vidal, *A generalized multi-scale entanglement renormalization ansatz: More accurate conformal data from a critical lattice model* (2022), [arxiv:arXiv:2212.06740](https://arxiv.org/abs/2212.06740).